# Adaptive noise reduction for power Doppler imaging using SVD filtering in the channel domain and coherence weighting of pixels

Baptiste Pialot, Célestine Lachambre, Antonio Lorente Mur, Lionel Augeul, Lorena Petrusca, Adrian Basarab, François Varray

# *Adaptive noise reduction for power Doppler imaging using SVD filtering in the channel domain and coherence weighting of pixels*

*Baptiste Pialot[1] – Célestine Lachambre[1] – Antonio Lorente Mur[1] – Lionel Augeul[2] – Lorena Petrusca[1] – Adrian Basarab[1] – François Varray[1]*

1 - Univ Lyon, INSA-Lyon, Université Claude Bernard Lyon 1, CNRS, Inserm, CREATIS UMR 5220, U1294, F-69621, Lyon, France

2 - INSERM UMR-1060, Laboratoire CarMeN, Université Lyon 1, Faculté de Médecine, Rockefeller, Lyon, France

**Abstract**

*Objective*: Ultrafast power Doppler (UPD) is an ultrasound method that can image blood flow at several thousands of frames per second. In particular, the high number of data provided by UPD enables the use of singular value decomposition (SVD) as a clutter filter for suppressing tissue signal. Notably, is has been demonstrated in various applications that SVD filtering increases significantly the sensitivity of UPD to microvascular flows. However, UPD is subjected to significant depth-dependent electronic noise and an optimal denoising approach is still being sought. *Approach*: In this study, we propose a new denoising method for UPD imaging: the Coherence Factor Mask (CFM). This filter is first based on filtering the ultrasound time-delayed data using SVD in the channel domain to remove clutter signal. Then, a spatiotemporal coherence mask that exploits coherence information between channels for identifying noisy pixels is computed. The mask is finally applied to beamformed images to decrease electronic noise before forming the power Doppler image. We describe theoretically how to filter channel data using a single SVD. Then, we evaluate the efficiency of the CFM filter for denoising *in vitro* and *in vivo* images and compare its performances with standard UPD and with three existing denoising approaches. *Main results*: The CFM filter gives gains in signal-to-noise ratio and contrast-to-noise ratio of up to 22 dB and 20 dB, respectively, compared to standard UPD and globally outperforms existing methods for reducing electronic noise. Furthermore, the CFM filter has the advantage over existing approaches of being adaptive and highly efficient while not requiring a cut-off for discriminating noise and blood signals nor for determining an optimal coherence lag. *Significance*: The CFM filter has the potential to help establish UPD as a powerful modality for imaging microvascular flows.

## 1 - Introduction

Ultrafast power Doppler (UPD) is a well-established ultrasound method for imaging blood flow at several thousands of frames per second [1]. In particular, the combination of advanced clutter filters such as singular value decomposition (SVD) filters with UPD enables the imaging of blood flows that were previously inaccessible to ultrasound [2]. Indeed, SVD performs spatiotemporal filtering of tissue signals that increases significantly the sensitivity of UPD to thin and slow blood flow [2]. Hence, it has been demonstrated that UPD combined with SVD filtering can image at a high frame rate microvascular flows in the brain, the optical system, or the spinal cord, among others [3]–[5]. In particular, the mean intensity of the power Doppler signal is generally accepted to be proportional to blood flow volume, making it possible to use UPD images to map brain activity in functional ultrasound [3]. However, due to acoustic attenuation, UPD images still remain subjected to a significant depth-dependent electronic noise, which degrades the signal-to-noise ratio (SNR) and contrast-to-noise ratio (CNR) in deep regions.

The standard framework for forming a UPD image is built upon the delay-and-sum (DAS) beamformer. In DAS beamforming, data acquired by each piezoelectric channel are first focalized on a

pixel grid by applying the proper delays in reception. Then, the focalized signals coming from each channel are summed in every pixel. For increasing SNR, DAS beamforming is usually performed for several tilted plane waves whose corresponding beamformed images are then compounded together. The SVD clutter-filtering is performed after all these operations by determining a singular value cut-off that allows one to isolate tissue signals. Finally, the UPD image is computed as the zero-lag autocorrelation, i.e., the incoherent sum of clutter-filtered images [6]–[8]. In addition to compounding, one possible approach for reducing noise is to change the computation of UPD images. Notably, Tremblay-Darveau *et al.* [9] demonstrated that UPD images can be partially denoised if they are computed using a non-zero-lag autocorrelation. Also, Stanziola *et al.* [10] and Huang *et al.* [7] improved SNR by forming UPD images from the cross-correlation of beamformed signals acquired by subgroups of channels and angles, respectively. These correlation methods provide a good noise reduction without increasing the computational complexity. However, correlating channels necessitates careful design in order to avoid degrading the point spread function (PSF) of the system, and correlating angles lowers the overall frame rate. Moreover, several noise equalization and noise debiasing methods performed directly on UPD images have been proposed [11]–[13]. Yet, it is important to mention that noise equalization does not actually improve the SNR but rather the flow visualization. For the compounding step, Kang *et al*. [8] showed that using nonlinear compounding gives better SNR and CNR in UPD images. Furthermore, an alternative for increasing the SNR can be to acquire the UPD raw radiofrequency (RF) data using coded excitations [14], [15]. However, this approach requires a careful design of the coded sequences as well as their associated decoding in reception. Lastly, contrast agents can be used to strongly enhance the signal of blood flow [16]. Notably, the non-linear properties of microbubbles can be exploited using harmonic or superharmonic imaging to visualize the slowest blood velocities that can be suppressed by SVD [17]. However, contrast imaging is an invasive procedure by nature.

Another possible approach for lowering noise in UPD images is to filter it using SVD in addition to tissue. Indeed, a singular value cut-off can also be determined to separate blood and noise signals in the spatiotemporal basis provided by SVD [6], [18]. However, since noise and blood signals are not perfectly decorrelated, this approach implies a trade-off between noise reduction and a full restitution of the blood flow [11], [19]. In addition, an optimal noise cut-off has to be determined. However, Song *et al.* (2017) demonstrated that these drawbacks can be partially compensated by a block SVD algorithm, which relies on local assumptions about noise and blood in images. Also, Ozgun et *al.* [19] proposed a higher-order SVD filtering of focalized signals before performing the channel summation that would complete the DAS process. In particular, these authors demonstrated that such a multidimensional filtering in the channel domain makes it possible to increase the noise reduction capacity of SVD. However, the higher-order SVD needs to determine multiple singular value cut-offs for blood and noise subspaces.

In addition to the higher-order SVD [17], few studies have used the channel domain to perform noise reduction in UPD imaging. Yet, although processing in the channel domain is computationally expensive, it gives access to additional information compared to operating on beamformed data only. This is one of the key aspects of the Coherent Flow Power Doppler (CFPD) beamformer [20], [21] that is based on clutter filtering of the time-delayed RF data in the channel domain before forming the power Doppler image as a channel short-lag spatial coherence (SLSC) map. Notably, it has been demonstrated that the CFPD beamformer reduces electronic noise and also diffuse moving clutter. However, SLSC has an inherent high computational complexity and requires experimental determination of the optimal lag [22].

In this study, we propose a method that combines SVD filtering in the channel domain and coherence weighting of beamformed images to significantly reduce noise in UPD imaging: the Coherence Factor Mask (CFM) filter. First, the RF data are focalized on a pixel grid and the compounding is performed without the channel summation. Next, focalized and compounded data

acquired by each channel are concatenated into a single matrix. Then, SVD clutter-filtering of tissue is performed on the concatenated matrix using a formalism denoted "Grouped Channel" (GC) SVD. Once the tissue signal is filtered using GC SVD, a channel Coherence Factor (CF) [23] is computed for each pixel of tissue-filtered channel data. Finally, the summation along channels is performed and the pixels of resulting beamformed images are multiplied by their corresponding CF. Given that the coherence along channels is lower for noise than for blood, the multiplication by the CF reduces the amplitude of pixels dominated by noise. Hence, a denoised UPD image can finally be computed from the CF-weighted set of beamformed images. The CFM filter is compared on *in vitro* data with several denoising approaches presented previously, and demonstrates its superior ability in reducing depth-dependent electronic noise. Also, with the CFM filter the UPD images of the coronaries of a pig can be strongly enhanced compared with standard UPD.

The paper is organized as follows. First, we recall the basics of standard UPD imaging with SVD filtering. Next, we present in detail three existing denoising approaches and the theory behind the proposed approach. Then, we describe the *in vitro* and *in vivo* experiments conducted for the comparison of the proposed method with existing approaches and standard UPD. We present the results of these experiments before ending the paper with a discussion and a conclusion about the presented work. Furthermore, some theoretical insights into SVD and GC SVD are provided in an Appendix at the end of the paper.

## 2 – Materials and Methods

### 2. 1 Basics of Ultrafast Power Doppler (UPD)

*a) Plane wave acquisitions*

Let us consider a 1D ultrasonic array with $n_e$ emitting and receiving channel. After reception, signals acquired at discrete time $t = \{1,2, \dots, n_t\}$ by each channel are IQ demodulated and focalized on a 2D pixel grid with indices $x = \{1,2, \dots, n_x\}$ and $z = \{1,2, \dots, n_z\}$ in lateral an axial direction, respectively. This focalization leads to $n_e$ 3D migrated channel tensors $\boldsymbol{\mathcal{M}}_i \in \mathbb{C}^{n_x,n_z,n_t}$ where $i = \{1,2, \dots, n_e\}$. To complete DAS beamforming, channel tensors are summed as follows:

$$\boldsymbol{\mathcal{B}} = \sum_{i=1}^{n_e} \boldsymbol{\mathcal{M}}_i \quad (1)$$

where $\boldsymbol{\mathcal{B}} \in \mathbb{C}^{n_x,n_z,n_t}$ is the tensor of DAS-beamformed images. Finally, for enhancing SNR, this DAS beamforming process is realized for several emission angles and the resulting beamformed tensors are compounded together.

*b) SVD*

To filter signals coming from tissues using SVD, the DAS-beamformed tensor $\boldsymbol{\mathcal{B}}$ is first reshaped into a spatiotemporal Casorati matrix $\boldsymbol{B} \in \mathbb{C}^{n_x n_z,n_t}$. The SVD of $\boldsymbol{B}$ is then:

$$\boldsymbol{B} = \boldsymbol{U}_B \mathbf{S}_B \boldsymbol{V}_B^* \quad (2)$$

where $\boldsymbol{U}_B \in \mathbb{C}^{n_x n_z,n_t}$ and $\boldsymbol{V}_B \in \mathbb{C}^{n_t,n_t}$ are unitary matrices and $\mathbf{S}_B \in \mathbb{C}^{n_t,n_t}$ is a diagonal matrix that contains the $n_t$ singular values $\sigma_i$ of $\boldsymbol{B}$; * stands for the conjugate transpose. Note that in ultrasound imaging the singular values are usually all distinct and sorted in $\mathbf{S}_B$ such that $\sigma_1 > \sigma_2 \dots > \sigma_{n_t}$. Also, as explained by Demené *et al.* [2], the columns of $\boldsymbol{V}_B$ contain the temporal singular vectors, which reflect all the temporal modes of the ultrasound data. Similarly, each column of $\boldsymbol{U}_B$ contains a set of pixels sharing the temporal characteristics that are contained in the corresponding column of $\boldsymbol{V}_B$.

Once the SVD of $\boldsymbol{B}$ has been computed, a rank reduction for filtering tissue signals is performed by setting to 0 the highest singular values. A denoising of $\boldsymbol{B}$ can also be performed by setting to 0 the small singular values, which correspond to noise.

*c) Standard Ultrafast Power Doppler (UPD)*

Let us denote by $\widehat{\boldsymbol{B}}$ the DAS-beamformed Casorati matrix where tissue signals have been removed with SVD. This matrix is reshaped into a tissue-filtered tensor $\widehat{\boldsymbol{\mathcal{B}}} \in \mathbb{C}^{n_x,n_z,n_t}$, and a standard UPD image $UPD \in \mathbb{R}^{n_x,n_z}$ with the following entries is finally computed:

$$UPD(x,z) = \sum_{t=1}^{n_t} \left|\widehat{\mathcal{B}}(x,z,t)\right|^2 \quad (3)$$

*d) Existing denoising methods*

We present in this section three denoising methods for UPD imaging that will be compared with the proposed method in the next sections. These methods are angle correlation [7], SVD noise-cut off as implemented by Song *et al.* [18], and CFPD beamformer [20], [21]. The methods were chosen because they represent three of the main categories of denoising approaches identified in the Introduction: noise reduction after beamforming and SVD, SVD-based denoising, and an alternative beamforming method.

*Angle correlation*

In angle correlation [7], images are separated into two non-overlapping subgroups following DAS beamforming and SVD tissue filtering. More precisely, each subgroup is made of images compounded from two different sets of angles. The UPD image $PD_{angle}$ is then formed as the cross-correlation of the two subgroups along slow time:

$$PD_{angle}(x,z) = \left|\sum_{t=1}^{n_t} \widehat{\mathcal{B}}_1(x,z,t)\,\widehat{\mathcal{B}}_2(x,z,t)^*\right| \quad (4)$$

where $\widehat{\mathcal{B}}_1(x,z,t)$ and $\widehat{\mathcal{B}}_2(x,z,t)$ are the entries of the SVD-filtered DAS tensors of the two subsets.

*SVD noise cut-off*

We consider here the method of Song *et al.* [18] for determining a cut-off that allows one to identify the singular values that correspond to noise. A summary of other proposed methods can be found in the study by Baranger *et al.* [6].

First, the beamformed and tissue-filtered tensor $\widehat{\boldsymbol{\mathcal{B}}}$ is formed. Then, using SVD, the Doppler frequency of each temporal singular vector in the column of $\boldsymbol{V}_B$ is computed from the respective autocorrelations. A preliminary singular value cut-off is identified by exploiting the change in Doppler frequency occurring between blood-dominated subspaces and noise-dominated subspaces. Then, this preliminary cut-off is used to identify the zone of the singular value curve that corresponds to the noise subspaces. Finally, the noise cut-off is determined from a linear fit of the singular value curve in that zone. The final UPD image is then computed as in equation (3).

*CFPD beamformer*

The CFPD beamformer [20], [21] operates in the channel domain on migrated channel tensors $\boldsymbol{\mathcal{M}}_i$. First, tissue signals are removed from these tensors using separate clutter filters such as SVD for

each channel. After the tissue-filtering, an SLSC tensor is computed from tissue-filtered tensors $\widehat{\boldsymbol{\mathcal{M}}}_i$ with entries:

$$SLSC(m,x,z,t) = \frac{1}{n_e - m} \sum_{i=1}^{n_e - m} \frac{\sum_{z=z_1}^{z_2} \widehat{\mathcal{M}}_i(x,z,t)\, \widehat{\mathcal{M}}_{i+m}(x,z,t)}{\sqrt{\sum_{z=z_1}^{z_2} \widehat{\mathcal{M}}_i^2(x,z,t) \sum_{z=z_1}^{z_2} \widehat{\mathcal{M}}_{i+m}^2(x,z,t)}} \quad (5)$$

where $\widehat{\mathcal{M}}_i(x,z,t)$ are the entries of filtered tensors $\widehat{\boldsymbol{\mathcal{M}}}_i$ and $m$ is the number of lags to consider.

The CFPD image $PD_{CFPD}$ is finally computed as:

$$PD_{CFPD}(x,z) = \sum_{t=1}^{n_t} \left( \sum_{m=1}^{N} SLSC(m,x,z,t) \right)^2 \quad (6)$$

where $N$ is the maximum number of lags on which the UPD image is computed.

**2. 2 Proposed denoising method**

The proposed denoising method consists of two main steps. First, tissue signals are removed from focalized and compounded data using a single SVD in the channel domain. Then, a denoising mask for the resulting beamformed images is computed from a channel domain coherence analysis.

*a) Grouped channel SVD (GC SVD)*

We propose to perform SVD filtering of tissue in the channel domain as in the CFPD beamformer [20], [21] and higher-order SVD [19]. However, contrary to higher-order SVD, we do not use multidimensional filtering of the data. Indeed, higher-order SVD filters tissue along the slow time but also along channels. This multidimensional filtering needs two cut-offs for isolating the tissue subspace: one for the slow-time direction and one for the channel direction. Here, we keep a cut-off along the slow time only. In CFPD beamforming, this SVD filtering along the slow-time direction is performed separately for each channel. Here, for more computational efficiency, we propose to perform SVD filtering on a single Casorati matrix, which is the concatenation of all channel data. We denote this grouped channel SVD by "GC SVD".

First, each channel tensor $\boldsymbol{\mathcal{M}}_i$ is reshaped into a Casorati matrix $\boldsymbol{M}_i \in \mathbb{C}^{n_x n_z, n_t}$. For each matrix $\boldsymbol{M}_i$, a compounding of several emission angles is realized for enhancing SNR. The concatenated Casorati matrix $\boldsymbol{M} \in \mathbb{C}^{n_e n_x n_z, n_t}$ is then formed as:

$$\boldsymbol{M} = \left[ \boldsymbol{M}_1 \dots \boldsymbol{M}_{n_e} \right]^T \quad (7)$$

Finally, the GC SVD of the channel data is:

$$\boldsymbol{M} = \boldsymbol{U}_M \boldsymbol{S}_M \boldsymbol{V}_M^* \quad (8)$$

where $\boldsymbol{S}_M$ and $\boldsymbol{V}_M$ are of the same dimensions as $\boldsymbol{S}_B$ and $\boldsymbol{V}_B$ and $\boldsymbol{U}_M \in \mathbb{C}^{n_e n_x n_z, n_t}$**.** As for $\boldsymbol{B}$, a rank reduction can be performed on $\boldsymbol{M}$ with GC SVD for filtering the tissue subspace. Then, the tissue-filtered matrix $\widehat{\boldsymbol{M}} \in \mathbb{C}^{n_e n_x n_z, n_t}$ is re-separated into tissue-filtered channel matrices $\widehat{\boldsymbol{M}}_i \in \mathbb{C}^{n_x n_z, n_t}$. Lastly, a channel summation is performed on matrices $\widehat{\boldsymbol{M}}_i$ to complete the beamforming process.

*b) Comparison of SVD and GC SVD*

One may ask whether the blood subspace in the SVD tissue-filtered matrix $\widehat{\boldsymbol{B}}$ can be recovered after the channel summation of matrices $\widehat{\boldsymbol{M}}_i$. This condition is indeed mandatory when using GC SVD as a channel-domain clutter filter. For this, we make the simplifying assumption that tissue, noise and

blood subspaces are perfectly orthogonal. As stated in the Introduction, this assumption is not perfectly true in practice, but it will help to understand the effect of GC SVD on tissue filtering. Let us denote:

$$\boldsymbol{U}_M = \left[(\boldsymbol{U}_M)_1 \dots (\boldsymbol{U}_M)_{n_e}\right]^T \quad (9)$$

with $(\boldsymbol{U}_M)_i \in \mathbb{C}^{n_x n_z, n_t}$ the 2D sub-matrix of $\boldsymbol{U}_M$ that contains all the spatial singular vectors relative to the i-th channel. The notation (9) is possible because GC SVD conserves the ordering of the channels in $\boldsymbol{U}_M$ like SVD conserves the spatial ordering of pixels in $\boldsymbol{U}_B$. Equations (7), (8), and (9) imply:

$$\boldsymbol{M} = \left[(\boldsymbol{U}_M)_1 \dots (\boldsymbol{U}_M)_{n_e}\right]^T \mathbf{S}_M \boldsymbol{V}_M^*$$

$$= \left[(\boldsymbol{U}_M)_1 \mathbf{S}_M \boldsymbol{V}_M^* \dots (\boldsymbol{U}_M)_{n_e} \mathbf{S}_M \boldsymbol{V}_M^*\right]^T$$

$$= \left[\boldsymbol{M}_1 \dots \boldsymbol{M}_{n_e}\right]^T (10)$$

From equation (10), one may note that $\boldsymbol{M}_i = (\boldsymbol{U}_M)_i \mathbf{S}_M \boldsymbol{V}_M^*$. However, $(\boldsymbol{U}_M)_i \mathbf{S}_M \boldsymbol{V}_M^*$ is not the SVD decomposition of $\boldsymbol{M}_i$.

Now, let us suppose that the tissue singular values in $\mathbf{S}_M$ are set to 0. Because $\boldsymbol{M}_i = (\boldsymbol{U}_M)_i \mathbf{S}_M \boldsymbol{V}_M^*$, each channel matrix $\boldsymbol{M}_i$ will be tissue-filtered using the same rank-reduction and the resulting tissue-filtered concatenated matrix $\widehat{\boldsymbol{M}}$ will be:

$$\widehat{\boldsymbol{M}} = \left[(\boldsymbol{U}_M)_1 \mathbf{S}_M^{b+n} \boldsymbol{V}_M^* \dots (\boldsymbol{U}_M)_{n_e} \mathbf{S}_M^{b+n} \boldsymbol{V}_M^*\right]^T$$

$$= \left[\widehat{\boldsymbol{M}}_1 \dots \widehat{\boldsymbol{M}}_{n_e}\right]^T (11)$$

where $\mathbf{S}_M^{b+n}$ (b: blood, n: noise) is the matrix $\mathbf{S}_M$ in which singular values corresponding to tissue have been set to 0. Next, the beamforming process is completed with the channel summation of matrixes $\widehat{\boldsymbol{M}}_i$ :

$$\widehat{\boldsymbol{B}}_{GC} = \sum_{i=1}^{n_e} \widehat{\boldsymbol{M}}_i = \left(\sum_{i=1}^{n_e} (\boldsymbol{U}_M)_i\right) \mathbf{S}_M^{b+n} \boldsymbol{V}_M^* \quad (12)$$

where $\widehat{\boldsymbol{B}}_{GC} \in \mathbb{C}^{n_x n_z, n_t}$ denotes the Casorati set of beamformed images obtained after GC SVD tissue-filtering and channel summation.

Based on developments presented in the Appendix section, we now assume that the following approximate equalities hold:

- $$\begin{cases} \mathbf{S}_M \approx \mathbf{S}_B \\ V_M^t \approx V_B^t \\ \mathrm{V}_M^b \approx V_B^b \end{cases} \quad (13)$$

where the exponent $t$ denotes the indices of columns in $\boldsymbol{V}_B$ that contain tissue signals and the exponent $b$ denotes columns with blood signals.

With equation (13) and by definition of SVD, one should have $\left(\sum_{i=1}^{n_e} (U_M^t)_i\right) \approx U_B^t$ and $\left(\sum_{i=1}^{n_e} \left(U_M^b\right)_i\right) \approx U_B^b$. Furthermore, if we denote by $\mathbf{S}_B^b$ and $\mathbf{S}_M^b$ the matrices $\mathbf{S}_B$ and $\mathbf{S}_M$ where tissue and noise singular values have been set to 0 and by $\mathbf{S}_B^n$ and $\mathbf{S}_M^n$ the same matrices but with tissue and blood singular values set to 0, equation (12) becomes:

$$\widehat{\boldsymbol{B}}_{GC} = \left(\sum_{i=1}^{n_e} (\boldsymbol{U}_M)_i\right) \boldsymbol{S}_M^{b+n} \boldsymbol{V}_M^*$$

$$= \left(\sum_{i=1}^{n_e} (\boldsymbol{U}_M)_i\right) \boldsymbol{S}_M^{b} \boldsymbol{V}_M^* + \left(\sum_{i=1}^{n_e} (\boldsymbol{U}_M)_i\right) \boldsymbol{S}_M^{n} \boldsymbol{V}_M^*$$

$$\approx \boldsymbol{U}_B \boldsymbol{S}_B^b \boldsymbol{V}_B^* + \boldsymbol{N} \quad (14)$$

Hence, GC SVD tissue-filtering followed by channel summation gives the same blood subspace $\boldsymbol{U}_B \boldsymbol{S}_B^b \boldsymbol{V}_B^*$ as SVD tissue-filtering plus a different noise subspace $\boldsymbol{N}$. However, one may note that each pixel in $\boldsymbol{N}$ will just be a different realization of the noise distribution of the corresponding pixel in $\boldsymbol{B}$. Based on these results, one can now use GC SVD to perform tissue filtering in the channel domain.

*c) CFM filtering of beamformed images*

Let us consider the $n_e$ tensors $\widehat{\boldsymbol{\mathcal{M}}}_i \in \mathbb{C}^{n_x, n_z, n_t}$ obtained after (1) focusing of RF data on a pixel grid, (2) compounding, (3) suppression of tissue signals using GC SVD, and (4) reshaping of the Casorati matrix. Because we now have access to the contribution of blood and noise in each pixel, one can compute a coherence factor weight $\boldsymbol{CF} \in \mathbb{C}^{n_x, n_z, n_t}$ whose entries are:

$$\boldsymbol{CF}(x,z,t) = \frac{\left|\sum_{i=1}^{n_e} \widehat{m}_i(x,z,t)\right|^2}{n_e \sum_{i=1}^{n_e} |\widehat{m}_i(x,z,t)|^2} \quad (15)$$

where $\widehat{m}_i(x,z,t)$ is the pixel in $\widehat{\boldsymbol{\mathcal{M}}}_i$ of coordinates $(x,z,t)$, which is the tissue-filtered pixel of coordinates $(x,z)$ acquired at discrete time $t$ by the i-th channel.

By definition, the entries of $\boldsymbol{CF}$ in equation (15) will be significantly higher for pixels that contain mostly blood because they are more coherent across channels than pixels that contain mostly noise. Hence, the tensor $\boldsymbol{CF}$ can be seen as a 3D denoising mask that makes it possible to enhance the contribution of pixels where blood signal is dominant. To avoid strong discontinuities between blood-dominated and noise-dominated pixels, a 2D Gaussian filtering with a standard deviation $\sigma$ is applied to the 3D mask $\boldsymbol{CF}$ at each discrete time $t$. The impact of the parameter $\sigma$ is detailed in the Results and Discussion sections. Then, the set of beamformed images obtained after GC SVD and channel summation is multiplied pixel-wise by the CF mask. Finally, a denoised UPD image is formed as in equation (3).

The aforementioned steps of the CFM filter are summarized in Figure 1 using the *in vivo* data presented in the next sections.

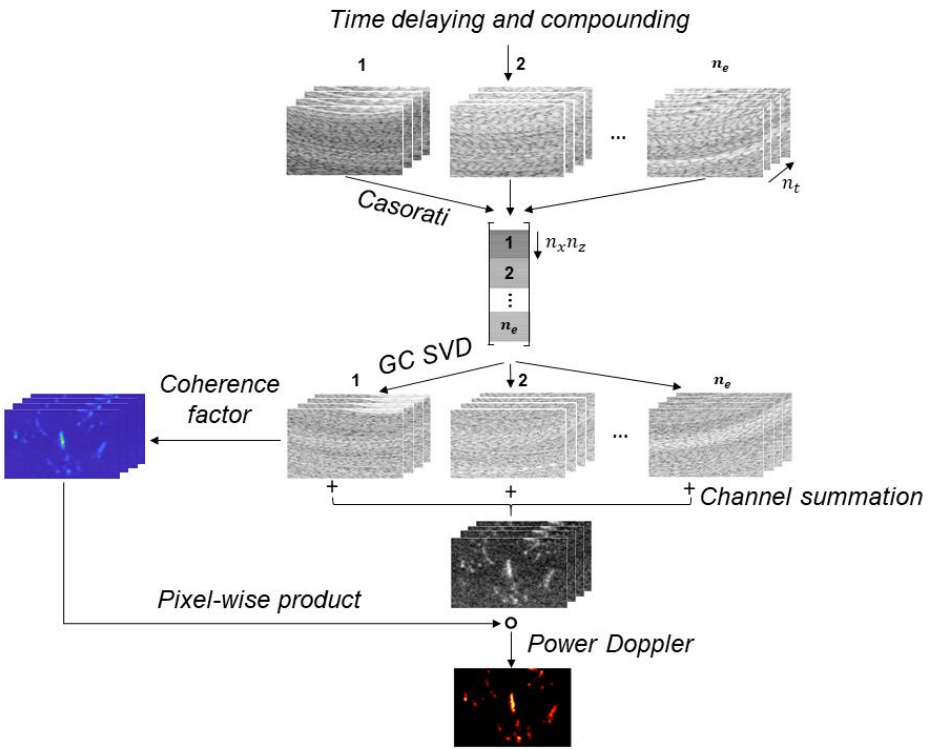


*Figure 1 – Graphical representation of the CFM filter. First, the raw RF data are time-delayed and compounded. Then, time-delayed and compounded data acquired by each channel are concatenated into a single Casorati matrix. The tissue signal is removed using GC SVD and the Casorati matrix is re-separated into SVD-filtered channel data. A pixel-wise coherence factor is then computed from the filtered channel data to obtain a spatiotemporal coherence mask. Next, the data from each channel are summed to complete the beamforming process and the resulting beamformed images are multiplied pixel-wise by the coherence mask for filtering noise. Finally, a denoised power Doppler image is formed from the set of noise-filtered images.*

## 3 - Experimental settings

*a)* In vitro *experiments*

*In vitro* acquisitions were performed using an L22-8 CMUT linear probe (128 elements, transmit frequency: 15.625 MHz). The probe was driven with a Vantage 256 research scanner (Verasonics, Kirkland, USA). The sampling frequency of the scanner was set to 62.5 MHz.

The experimental phantom consisted in a tissue-mimicking layer molded around a PVC tube (inner diameter: 1.5 mm, outer diameter: 2.1 mm) in a plastic box. The tissue-mimicking layer was composed of agar (2% of its mass), silica powder (1%), and water (97%). First, the PVC tube was inserted and glued through holes perforated in the box at 25 mm deep. Then, some ultrasound gel was added around the tube to ensure good coupling with the tissue-mimicking layer. Finally, the tissue-mimicking layer was melted at 80°C and then slowly pounded in the box.

A mixture of water and cellulose was used to mimic flowing scatterers inside the tube of the phantom. The flow rate was imposed at the entrance of the tube using a syringe pump (InfusionOne,

New Era Pump Systems, New York, USA). During ultrasound acquisitions, the phantom was immerged in a water bath.

Three types of ultrasound experiments were conducted on the phantom: longitudinal acquisitions with the probe parallel to the flow axis, transversal acquisitions with the probe perpendicular to the flow, and freehand acquisitions with the probe held parallel to the flow by hand. The freehand acquisitions were made to mimic a more realistic imaging situation, with moving clutter in addition to electronic noise. For the longitudinal and transversal experiments, four flow rates were investigated with values of 0.5 $mL.min^{-1}$, 1 $mL.min^{-1}$, 2 $mL.min^{-1}$, and 4 $mL.min^{-1}$, corresponding to a theoretical mean flow velocity of 4.7 $mm.s^{-1}$, 9.4 $mm.s^{-1}$, 18.8 $mm.s^{-1}$ and 37.6 $mm.s^{-1}$, respectively. Five sets of 128 frames were acquired for each flow rate. For freehand acquisitions, three sets of 128 frames were acquired at a flow rate of 1 $mL.min^{-1}$. The Pulse Repetition Frequency (PRF) of longitudinal and transversal experiments was set to 500 Hz and the PRF for freehand experiments was set to 50 Hz for capturing hand movements. For all experiments, nine plane waves were used with compounding angles ranging from -4° to 4° with a step of 1°. An additional longitudinal experiment at a flow rate of 2 $mL.min^{-1}$ was conducted with 17 angles ranging from -8° to 8° to evaluate how the number of compounding angles impacts the denoising methods.

b) In vivo *experiments*

The *in vivo* data were acquired with a Vantage 256 scanner (Verasonics, Kirkland, USA) using an L12-5 linear probe (Philips, Amsterdam, Netherlands) having 256 elements and a central frequency of 7.8 MHz. The sampling frequency of the scanner was set to 62.5 MHz. Three compounding angles were used and the PRF between each compounded image was 9000 Hz. The probe was positioned at the surface of the heart of a pig during an open-chest experiment to acquire UPD images of the coronaries. Due to strong movements of the heart, UPD images were assessed using windows of 16 frames.

One should note that we did not use the same probe for *in vitro* and *in vivo* experiments. Indeed, we chose the CMUT transducer for *in vitro* experiments because the strong acoustic attenuation that occurs at 15 MHz allowed us to have a high level of electronic noise in power Doppler images. For *in vivo* experiments, we had to use a lower frequency in order to obtain an exploitable imaging depth. Also, we wanted to evaluate with at least two different imaging frequencies whether the RF data can be clutter-filtered in the channel domain.

*c) Post processing*

All acquired RF data were first IQ-demodulated. The IQ data were then time-delayed and projected on a pixel grid to obtain the migrated channel tensors $\boldsymbol{\mathcal{M}}_i$. These tensors were finally summed along the channel direction to obtain the DAS-beamformed tensor $\boldsymbol{\mathcal{B}}$ as in equation (1). A detailed explanation of the whole beamforming process can be found in the study by Perrot *et al* [24]. However, one should note that we did not use the matrix formulation of DAS to separate the time-delaying and channels summation steps.

To remove tissue signals, all cut-offs were the same for SVD and GC SVD. The cut-offs ranged between the second and the third singular value for longitudinal and transversal experiments and were equal to 19, 30, and 35 for the three freehand acquisitions. For *in vivo* data, the cut-off was set to the seventh singular values for all experiments.

In all of the experiments, the standard deviation of the Gaussian smoothing in the CFM filter was set to 1 pixel.

The SVD noise cut-offs computed with the method of Song *et al.* [18] in the longitudinal experiments were $22\pm4$, $34\pm1$, $52\pm1$, and $64\pm3$ for a flow rate of 0.5 $mL.min^{-1}$, 1 $mL.min^{-1}$, 2 $mL.min^{-1}$, and 4 $mL.min^{-1}$, respectively. For the transversal experiments, the cut-offs were $20\pm3$, $32\pm1$, $48\pm1$,

59±2 for the same flow rates and for the freehand experiments the cut-offs were 70, 84, and 65 for the three acquisitions at 1 mL.min$^{-1}$.

The number of lags for the CFPD beamformer was chosen to $N$=10 for the longitudinal and freehand experiments as this value maximized the SNR and CNR of the corresponding power Doppler images. However, with such a number of lags, a distortion of flow was observed in images for the transversal and *in vivo* experiments. To have the best compromise between good quality metrics and low flow distortion, we had to increase the number of lags to $N$=64 for the transversal experiment and to $N$=16 for the *in vivo* experiment. Furthermore, we selected $z = z_1 = z_2$ for all experiments.

*d) Quality metrics*

The efficiency of the different denoising methods was quantified with signal-to-noise ratio (SNR) and contrast-to-noise ratio (CNR) on UPD images. The SNR quantifies the amplitude of the selected signal region of interest (ROI) compared to the noise ROI. The CNR quantifies the contrast of the signal ROI compared to the noise ROI standard deviation.

$$SNR = 10\log\left(\frac{\sqrt{\frac{1}{N}\sum_{i=1}^{N} I_s^2(i)}}{\sqrt{\frac{1}{N}\sum_{i=1}^{N} I_n^2(i)}}\right) \quad (16)$$

$$CNR = 10\log\left(\frac{|\mu_s - \mu_n|}{\sigma_n}\right) \quad (17)$$

with $I_n$ the UPD image in the noise ROI, $I_s$ the UPD image in the signal ROI, $\mu_n$ and $\mu_s$ their respective mean, and $\sigma_n$ the standard deviation of noise.

For *in vitro* data, the signal ROI was selected from the B-mode image and covered the whole inner tube. The noise ROI was selected by translating the signal ROI under the tube to the greatest depth available.

For *in vivo* data, the signal ROI was manually selected in flow regions that were clearly visible with all denoising methods. The noise ROI was selected by translating the signal ROI at the greatest depth available such as for *in vitro* data.

**4 – Results**

Figure 2 describes how the Gaussian standard deviation $\sigma$ impacts the CFM filter. The line (A) shows denoising masks computed from the $\boldsymbol{CF}$ in equation (15) as a function of $\sigma$. All denoising masks have been averaged along slow time for better visualization. The line (B) shows the corresponding power Doppler images after CFM filtering. Finally, the graph (C) displays the CNR and SNR measured in the images of (B) as a function of $\sigma$. As expected, we can see in (A) that flow pixels exhibit a coherence factor higher than noise pixels by several decibel. Also, it can be seen in the masks that the coherence factor mitigates some incoherent imaging artifacts present at the top of the flow, which are most likely due to the wall of the measurement tube. The Gaussian filtering provides a smoothing of the denoising masks, which homogenizes locally the coherence factor in flow, noise, and artifact regions. However, if the Gaussian filtering is too aggressive, the smoothing blurs the denoising masks, as can be seen when $\sigma$>1 pixel. In (B) and (C), we can see how the Gaussian filtering affects the power Doppler images computed from the various denoising masks. The SNR and CNR increase with $\sigma$ up to $\sigma$=1 pixel thanks to the homogenization of the coherence factor provided by Gaussian smoothing. However, when $\sigma$>1 pixel, the SNR decreases with $\sigma$ and the CNR stays approximatively constant. Furthermore, the power Doppler images get progressively blurred causing a loss of spatial resolution.

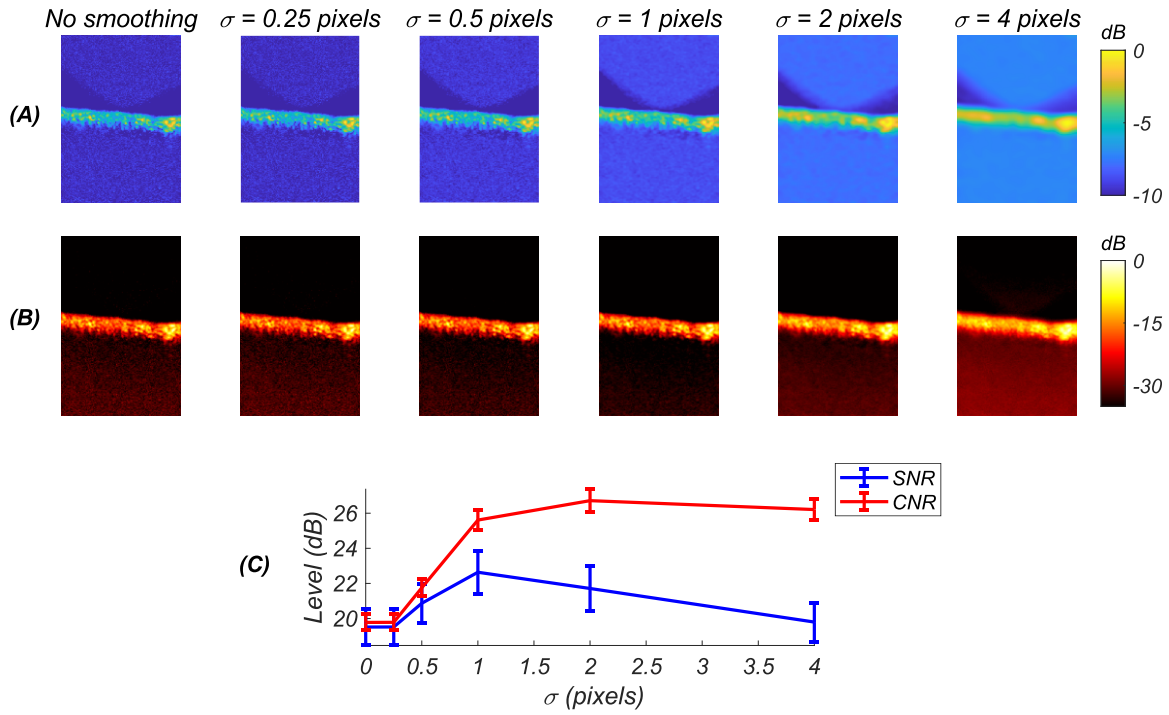


*Figure 2 – (A) Denoising masks computed from the coherence factor and after a Gaussian smoothing of standard deviation σ. (B) Power Doppler images denoised using the various denoising masks. (C) SNR and CNR in power Doppler images as a function of the standard deviation σ.*

Figure 3 shows power Doppler images produced from the different processing and denoising methods. The images in line (A), (B), and (C) have been acquired in longitudinal, transversal, and freehand phantom experiments, respectively. Globally, all methods enable denoising of the images compared with the standard UPD approach but not with the same efficiency. The SVD cut-off and angle correlation approaches provide a moderate reduction of noise in all experiments. Furthermore, the angle correlation produces grainy images thus limiting the gain of contrast provided by the denoising. However, it is evident that angle correlation mitigates more the movement artifacts at the top of the freehand images in (C) compared with the SVD cut-off. In comparison, the CFPD beamformer and the CFM filter provide strong noise reduction in all experiments. In particular, the CFPD beamformer gives an excellent contrast between the flow and background in the longitudinal experiments. However, its noise reduction capacity is lower in the transversal experiments because of the higher number of lags (64 instead of 10) used for its computation. Despite the high number of lags, it can be seen that the CFPD beamformer still slightly distorts the transversal flow. Also, in freehand experiments, the CFPD beamformer enhances some unwanted artifacts at the top of the flow that are similar to those that are attenuated by the CFM filter in Figure 2. Overall, the CFM filter provides a significant reduction in the depth-dependent noise in all the experiments without distorting the flow. However, it can be seen in the transversal experiments that the CFM filter enhances more the pixels in the center of the flow. This behavior causes the flow in the transversal experiments to appear less homogeneous when the CFM filter is used.

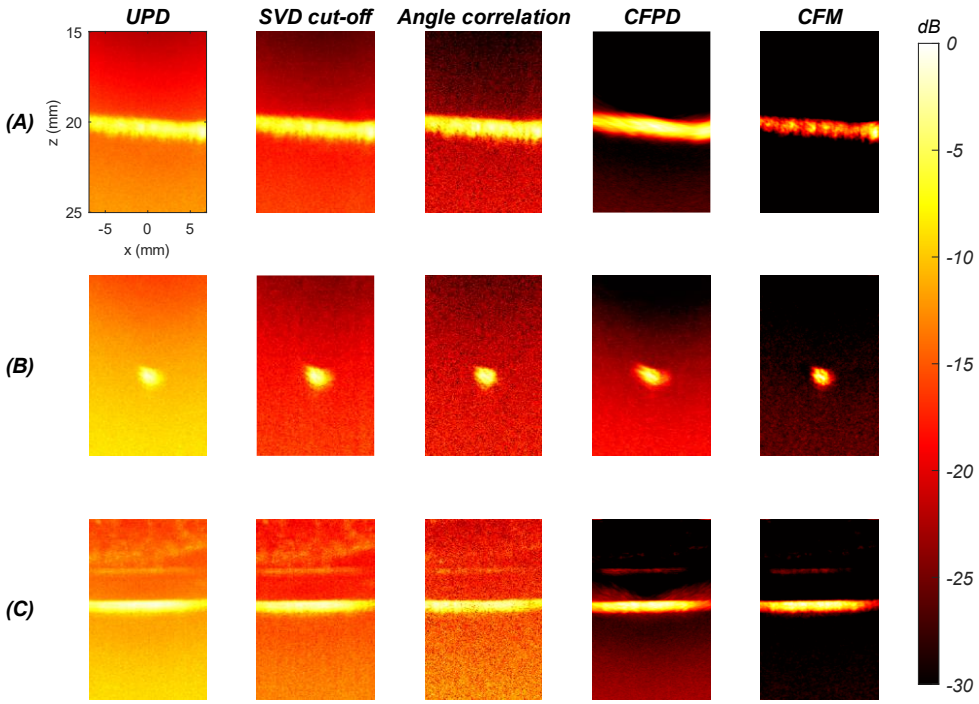


*Figure 3 – (A) Power Doppler images from the longitudinal phantom experiment computed using the various methods. (B) Power Doppler images from the transversal phantom experiment. (C) Power Doppler images from the freehand phantom experiment.*

Figure 4 displays box-and-whisker plots of the SNR (longitudinal: A, transversal: B, and freehand: C) and CNR (longitudinal: E, transversal: F, and freehand: G) computed for power Doppler images acquired in phantom experiments. The box-and-whisker plots have been computed for all flow rates, that is, five acquisitions per four flow rates for longitudinal and transversal cases and three acquisitions for only one flow rate for the freehand case. Figure 4 (D) and (H) also show the SNR and CNR gains obtained with each denoising methods compared with UPD. These gains have been averaged on all *in vitro* acquisitions, that is, longitudinal+transversal+freehand experiments. The box-and-whisker plots show that the best SNR enhancement is on average obtained with the CFM filter in all experiments, even if the performance of the CFPD beamformer is close in the longitudinal (A) and freehand (C) cases. As already observed in Figure 3, SVD cut-off and angle correlation generally give lower SNR enhancement than the CFPD and CFM approaches. The only exception is for the transversal experiments (B) where angle correlation and CFPD have a close performance because the efficiency of the CFPD in terms of SNR is decreased by the high number of lags. Globally, angle correlation provides a better SNR compared with SVD cut-off, except in the freehand experiments where both methods are close to UPD. Overall, the denoising methods provide an SNR gain over standard UPD in (D) of $4.1 \pm 2.0$ dB, $6.5 \pm 1.1$ dB, $10.4 \pm 3.3$ dB, and $14.5 \pm 1.9$ dB for SVD cut-off, angle correlation, CFPD, and CFM, respectively. For the CNR, the CFPD beamformer and the CFM filter also offer a significant improvement compared with the SVD cut-off and angle correlation. However, in the longitudinal experiments (E), the CNR is globally better for the CFPD than for the CFM and both approaches are roughly equivalent in terms of CNR in the freehand experiments (G). Again, the CFPD beamformer performs worse than the CFM filter in the transversal experiments (F). SVD cut-off and angle correlation provide negligible to small improvements in terms of CNR over standard UPD depending on the experiment. Overall, the denoising

methods provide a CNR gain over standard UPD in (H) of 3.2±1.8 dB, 1.5±1.4 dB, 10.0±3.4 dB, and 11.7±1.1 dB for SVD cut-off, angle correlation, CFPD, and CFM, respectively.

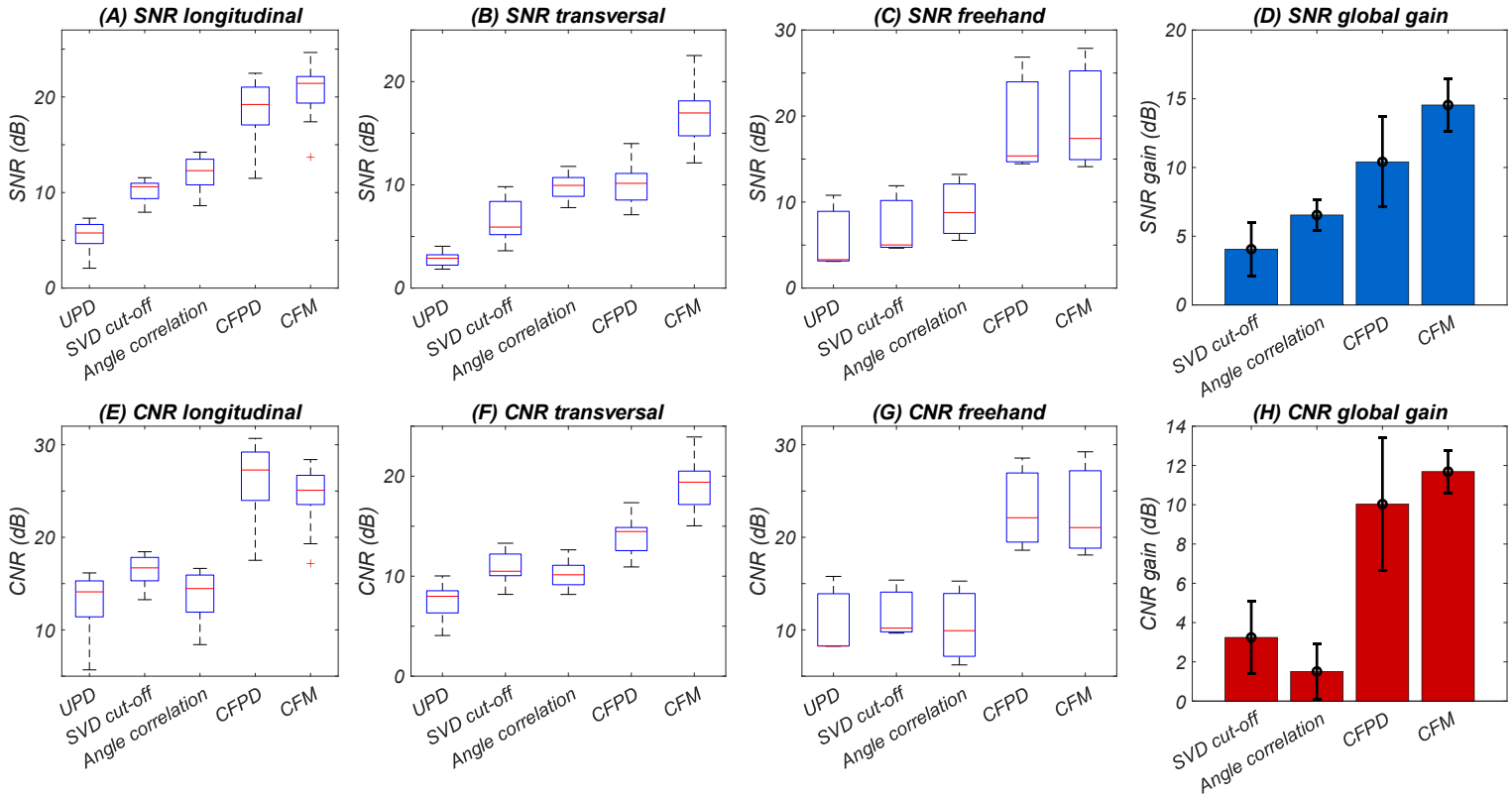


*Figure 4 – (A)-(B)-(C) SNR for power Doppler images from longitudinal, transversal, and freehand phantom experiments using the various approaches. (E)-(F)-(G) CNR for power Doppler images from longitudinal, transversal, and freehand experiments using the various approaches. (D)-(H) SNR and CNR gains of all denoising methods over standard UPD. The gains have been averaged on the three types of phantom experiments.*

Figure 5 shows how SNR and CNR evolve as a function of compounding angles for a longitudinal experiment performed at 2 mL.min$^{-1}$. As expected, both metrics increase with the number of angles for all methods except for the angle correlation, for which the SNR stays roughly constant and the CNR decreases slightly. Similar trends are observed to those in Figure 4 (A) with the CFM filter that gives the best SNR for all number of angles followed closely by the CFPD beamformer and inversely for the CNR. However, it is worth noting that the CFM filter has a better CNR than the CFPD beamformer when 17 compounding angles are used (A).

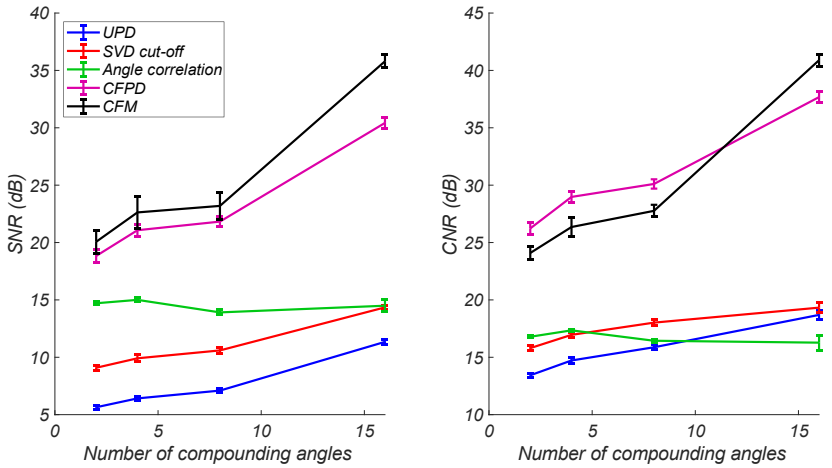


*Figure 5 – SNR (left) and CNR (right) of a longitudinal experiment as a function of the number of compounding angles.*

Figure 6 presents the power Doppler images acquired *in vivo* during the open-chest experiment. The three lines (A), (B), and (C) correspond to three sets of images acquired at different times during the experiment. As with the phantom data, SVD cut-off and angle correlation present a reduction of the depth-dependent noise, which is quite limited. In all experiments, the CFPD beamformer has a better performance but presents some unwanted artifacts in (C), most likely due to movements during acquisitions. The CFM filter reduces significantly the depth-dependent noise in comparison with all the other approaches without altering the vasculature.

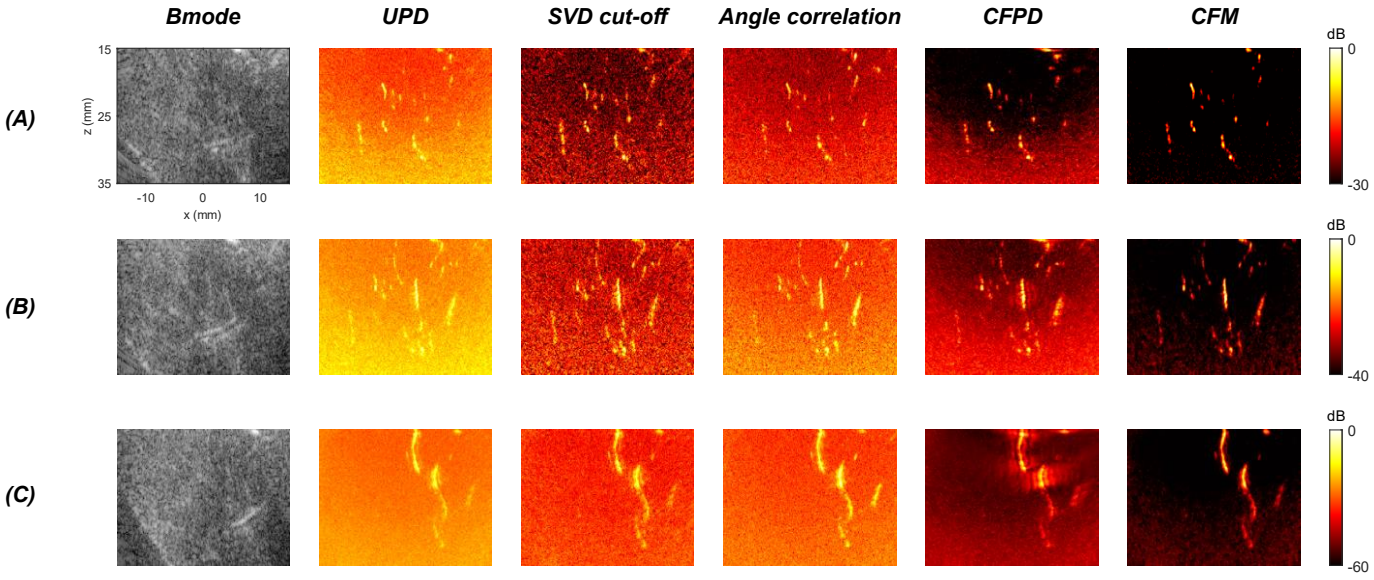


*Figure 6 – B-mode and corresponding power Doppler images computed with the various approaches for the open-chest experiment. (A), (B), and (C) correspond to acquisitions made at three different times during the experiment.*

Figure 7 shows the SNR and CNR measured from *in vivo* power Doppler images for all methods. Figure 7 also shows the signal and noise ROI used for SNR and CNR computation. The CFM outperforms all the other denoising methods for the computed metrics. The CFPD beamformer gives significantly better SNR and CNR compared with the SVD cut-off and angle correlation, which both provide small improvements compared with standard UPD. Overall, the denoising methods provide an

SNR gain over standard UPD of 6.0±1.3 dB, 4.0±2.3 dB, 11.3±4.4 dB, and 22.1±5.5 dB for SVD cut-off, angle correlation, CFPD, and CFM, respectively. The CNR gain is 3.4±1.6 dB, 2.5±1.7 dB, 10.1±3.4 dB, and 19.7±4.3 dB for SVD cut-off, angle correlation, CFPD, and CFM, respectively.

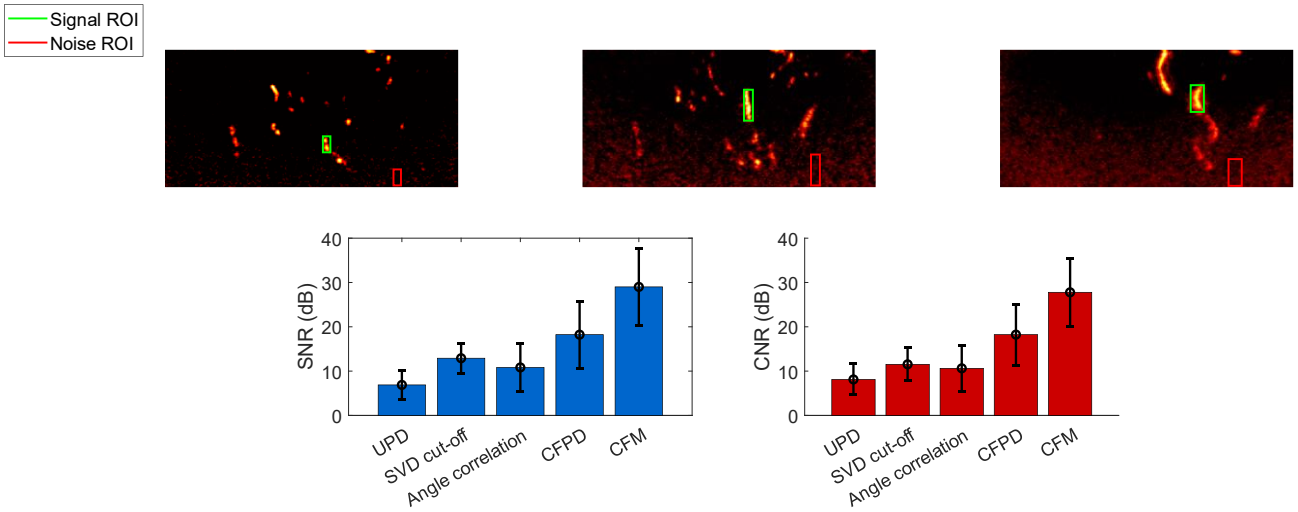


*Figure 7 – SNR and CNR measured for the* in vivo *experiment. The metrics are computed on the three sets of acquisitions presented in Figure 6. The signal and noise ROI are indicated on the corresponding CFM images.*

Finally, Figure 8 illustrates how the mean power Doppler intensity in CFM and UPD images evolves as a function of the flow rate in the longitudinal experiments. The mean intensity is normalized between 0 and 1 and has been computed using the signal mask defined for the quality metrics. It can be seen that both the CFM filter and standard UPD exhibit very similar intensity variations as a function of the flow rate.

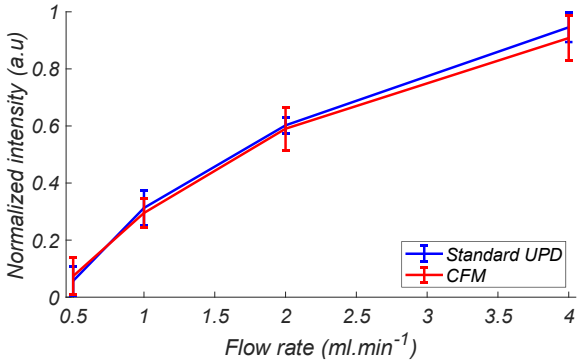


*Figure 8 – Variations of mean power Doppler intensity as a function of the flow rate in UPD and CFM images.*

## 5 – Discussion

We introduced in this study a new filtering approach for reducing electronic noise in UPD images: the CFM filter. This filter is based on filtering the RF data in the channel domain using grouped channel SVD (GC SVD) to remove clutter signal. Then, a pixel-wise coherent factor is computed from clutter-filtered channel data and used to generate a denoising mask that weighs the pixels of beamformed images. This weighting reduces the amplitude of noisy pixels thanks to their lowest coherent factor compared with blood pixels, thus strongly enhancing the quality of the final power Doppler image. The performance of the CFM filter was compared *in vitro* and *in vivo* with standard UPD and with three

other denoising methods: angle correlation [7], SVD noise cut-off [18], and CFPD beamformer [20], [21].

It is challenging to compare different denoising approaches for UPD imaging, and this study does not claim to be an exhaustive comparison of the investigated methods. Indeed, a study with more data and types of noise, clutter, and artifacts would be necessary to fully understand the pros and cons of each filter. However, we can propose some data-driven interpretations for the reduction of depth-dependent electronic noise. Overall, angle correlation [7] provided a noteworthy gain in SNR but a very limited gain in CNR, even when increasing the number of angles. This moderate performance can be expected since angle correlation exploits less information than denoising methods based on SVD or signal coherence. However, angle correlation has a very low computational complexity and is straightforward to implement. The SVD noise cut-off method [18] also showed a limited denoising capacity in terms of SNR and CNR. This can be explained by the fact that methods based on SVD noise cut-off assume that blood and noise subspaces are orthogonal. Thus, in practice, the consequent amount of noise that overlaps with blood in the SVD subspaces cannot be reduced by these methods without losing blood signal. More generally, the SVD noise cut-off cannot suppress, without losing blood signal, any artifact that shares the same subspaces as blood, such as the incoherent artifacts considered in the study by Huang *et al.* [7]. Nonetheless, as mentioned in the Introduction, it is important to note that advanced SVD algorithms such as block SVD [18] and higher-order SVD [19] possess better noise reduction capabilities than standard SVD. The CFPD beamformer is the only method that gave metrics close to or even better than the CFM filter in some experimental configurations. However, a comparison of the two approaches is difficult because of the flow distortions that CFPD caused in some data, which in turn impacted the choice of the optimal number of lags for the method. Also, it has been demonstrated that the CFPD beamformer is efficient for removing other types of unwanted signals than electronic noise such as reverberation artifacts [20]. As such artifacts are out of the scope of this study, we cannot offer a general conclusion on the comparison between the performance of the CFPD and the CFM. However, our results tend to prove that the CFM filter is better than the CFPD beamformer for removing noise that is purely electronic. Also, compared to the CFPD beamformer, the CFM filter has a much lower computational cost once the channel RF data are filtered, and it has a more versatile setting as well. Indeed, the only hyperparameter of the CFM filter is the standard deviation of the Gaussian smoothing, and its value was kept fixed during all of the experiments.

A potential limitation of the CFM filter is that the denoising mask can over-attenuate the flow regions that have a relatively low coherence factor. This behavior can be seen in the transversal power Doppler images of Figure 2 (B). However, this unwanted effect can be mitigated by reducing the standard deviation of the Gaussian smoothing that occurs in the filter. Also, the computational cost of the GC SVD, which is $O(n_e \times n_x \times n_z \times n_t^2)$ [23], is a general limitation of all denoising methods that exploit the channel domain RF data. However, a randomized algorithm for computing GC SVD could reduce its computational time to $O\left(n_e \times n_x \times n_z \times n_t \times log(k)\right)$, where $k$ is the number of singular values corresponding to the tissue subspace [25], [26]. Notably, such randomized algorithms have enabled real-time ultrasound imaging using conventional SVD filtering [26].

As mentioned in the Introduction, the mean power Doppler intensity in UPD images is proportional to blood flow volume and hence is of considerable interest in functional ultrasound imaging [3]. For the CFM filter, Figure 8 tends to prove that the pixel-wise weighting of the denoising mask preserves the same intensity variations as standard UPD. In other words, the increase of intensity in a flow pixel does not impact the relative amplitude of its coherence factor. This result suggests that the mean power Doppler intensity in images denoised by the CFM filter should also be proportional to blood flow volume. These observations will have to be confirmed in future *in vivo* studies. Also, the mean intensity of flow pixels in CFM images can be impacted by the Gaussian smoothing of the denoising mask. In particular, the pixels at the borders of the flow can have their intensity decreased by the presence of

neighboring noise pixels. With the decreased SNR observed in Figure 2 when $\sigma$ >1, this is an additional reason to perform only a slight Gaussian smoothing of the denoising mask.

The number of frames used for the computation of power Doppler images *in vivo* is limited and does not represent the true capabilities of the UPD method. However, using such a short ensemble has the advantage of providing a strong electronic noise and thus a good environment in which to evaluate the different denoising methods. Interestingly, the strong denoising provided by the CFM filter proves that the approach can be used to acquire denoised power Doppler images with short ensembles of frames. This result is of interest for reducing the ensemble lengths used *in vivo*, thus potentially avoiding some movement artifacts. Nonetheless, more *in vivo* experiments will be needed to evaluate the CFM filter and in particular experiments realized on larger ensembles of frames. Also, another limitation of the *in vivo* experiment is that a single animal has been used. Data should be acquired on several animals or organs to ensure a fully meaningful comparison between the denoising methods.

The theoretical framework presented for GC SVD shows that its equivalence with SVD mainly depends on the coherence between acquisition channels. Indeed, it is because ultrasound channels acquire data with a similar temporal content that it is reasonable to assume that SVD and GC SVD decompositions have similar singular values and singular vectors. Of course, we do not demonstrate here that SVD and GC SVD will always be strictly equivalent. However, we think that the coherence between channels should generally be sufficient for filtering tissue signals in the channel domain, as supported by our results. Also, it is worth mentioning that GC SVD is mode 2 of the higher-order SVD proposed by Ozgun *et al.* [19]. However, in this last study, the authors enhanced the intrinsic performance of SVD filtering and did not use an additional denoising method.

Finally, as stated in the introduction, UPD imaging is a powerful modality for imaging vascular and microvascular phenomena at a high frame rate in the human body. The CFM filter is of significant interest for the field, since lower electronic noise leads to more exploitable power Doppler images for the clinician. In turn, UPD could greatly help in the detection and diagnosis of microvascular diseases.

## 6 – Conclusion

This study introduced the CFM filter, a new approach for denoising ultrafast power Doppler images. The CFM filter combines clutter filtering in the channel domain and weighting of pixels using the coherence factor in order to drastically lower electronic noise. The feasibility of the CFM filter was demonstrated on *in vitro* and *in vivo* data. A comparison with three existing methods demonstrated its strong performance in terms of SNR and CNR. The CFM filter has great potential to help establish UPD imaging as a powerful modality for detecting and diagnosing microvascular diseases.

## 7 – Acknowledgments

This work was supported by the FEDER project MenisCare. It was also performed within the framework of the LABEX PRIMES (ANR-11-LABX-0063) of the Université de Lyon, within the programme ‘Investissements d’Avenir’ (ANR-11-IDEX-0007), operated by the French National Research Agency (ANR). This material is based upon work done on the PILoT facility (PILoT, INSA-Lyon). The RF Verasonics generator was cofounded by the FEDER program, Saint-Etienne Metropole (SME) and Conseil General de la Loire (CG42) within the framework of the SonoCardio-Protection Project leaded by Pr Pierre Croisille.

## 8 – Ethical Statement

The open-chest experiment was approved by the Animal Ethical Committee with agreement number 22090-2019092310275126.

## 9 – References

[1] J. Bercoff *et al.*, « Ultrafast compound Doppler imaging: providing full blood flow characterization », *IEEE Trans. Ultrason. Ferroelectr. Freq. Control*, vol. 58, nº 1, p. 134-147, jan. 2011, doi: 10.1109/TUFFC.2011.1780.

[2] C. Demené *et al.*, « Spatiotemporal Clutter Filtering of Ultrafast Ultrasound Data Highly Increases Doppler and fUltrasound Sensitivity », *IEEE Trans. Med. Imaging*, vol. 34, nº 11, p. 2271-2285, nov. 2015, doi: 10.1109/TMI.2015.2428634.

[3] T. Deffieux, C. Demené, et M. Tanter, « Functional Ultrasound Imaging: A New Imaging Modality for Neuroscience », *Neuroscience*, vol. 474, march 2021, doi: 10.1016/j.neuroscience.2021.03.005.

[4] R. Urs, J. A. Ketterling, et R. H. Silverman, « Ultrafast Ultrasound Imaging of Ocular Anatomy and Blood Flow », *Invest. Ophthalmol. Vis. Sci.*, vol. 57, nº 8, p. 3810-3816, july 2016, doi: 10.1167/iovs.16-19538.

[5] J. Claron *et al.*, « Large-scale functional ultrasound imaging of the spinal cord reveals in-depth spatiotemporal responses of spinal nociceptive circuits in both normal and inflammatory states », *Pain*, vol. 162, nº 4, p. 1047, 2021.

[6] J. Baranger, B. Arnal, F. Perren, O. Baud, M. Tanter, et C. Demené, « Adaptive Spatiotemporal SVD Clutter Filtering for Ultrafast Doppler Imaging Using Similarity of Spatial Singular Vectors », *IEEE Trans. Med. Imaging*, vol. PP, p. 1-1, feb. 2018, doi: 10.1109/TMI.2018.2789499.

[7] C. Huang *et al.*, « Simultaneous Noise Suppression and Incoherent Artifact Reduction in Ultrafast Ultrasound Vascular Imaging », *IEEE Trans. Ultrason. Ferroelectr. Freq. Control*, vol. 68, nº 6, p. 2075-2085, june 2021, doi: 10.1109/TUFFC.2021.3055498.

[8] J. Kang, D. Go, I. Song, et Y. Yoo, « Ultrafast Power Doppler Imaging Using Frame-Multiply-and-Sum-Based Nonlinear Compounding », *IEEE Trans. Ultrason. Ferroelectr. Freq. Control*, vol. 68, nº 3, p. 453-464, march 2021, doi: 10.1109/TUFFC.2020.3011708.

[9] C. Tremblay-Darveau *et al.*, « Improved Contrast-Enhanced Power Doppler Using a Coherence-Based Estimator », *IEEE Trans. Med. Imaging*, vol. 36, nº 9, p. 1901-1911, sept. 2017, doi: 10.1109/TMI.2017.2699672.

[10] A. Stanziola, C. H. Leow, E. Bazigou, P. D. Weinberg, et M.-X. Tang, « ASAP: Super-Contrast Vasculature Imaging Using Coherence Analysis and High Frame-Rate Contrast Enhanced Ultrasound », *IEEE Trans. Med. Imaging*, vol. 37, nº 8, p. 1847-1856, aug. 2018, doi: 10.1109/TMI.2018.2798158.

[11] P. Song, A. Manduca, J. D. Trzasko, et S. Chen, « Noise Equalization for Ultrafast Plane Wave Microvessel Imaging », *IEEE Trans. Ultrason. Ferroelectr. Freq. Control*, vol. 64, nº 11, p. 1776-1781, nov. 2017, doi: 10.1109/TUFFC.2017.2748387.

[12] R. Nayak, M. Fatemi, et A. Alizad, « Adaptive background noise bias suppression in contrast-free ultrasound microvascular imaging », *Phys. Med. Biol.*, vol. 64, nº 24, p. 245015, dec. 2019, doi: 10.1088/1361-6560/ab5879.

[13] C. Huang, P. Song, P. Gong, J. D. Trzasko, A. Manduca, et S. Chen, « Debiasing-Based Noise Suppression for Ultrafast Ultrasound Microvessel Imaging », *IEEE Trans. Ultrason. Ferroelectr. Freq. Control*, vol. 66, nº 8, p. 1281-1291, aug. 2019, doi: 10.1109/TUFFC.2019.2918180.

[14] E. Tiran *et al.*, « Multiplane wave imaging increases signal-to-noise ratio in ultrafast ultrasound imaging », *Phys. Med. Biol.*, vol. 60, nº 21, p. 8549-8566, nov. 2015, doi: 10.1088/0031-9155/60/21/8549.

[15] B. Pialot, A. Bernard, H. Liebgott, et F. Varray, « Sensitivity enhancement using chirp transmission for an ultrasound arthroscopic probe », *IEEE Trans. Ultrason. Ferroelectr. Freq. Control*, vol. PP, march 2022, doi: 10.1109/TUFFC.2022.3160880.

[16] Y. Desailly, A.-M. Tissier, J.-M. Correas, F. Wintzenrieth, M. Tanter, et O. Couture, « Contrast enhanced ultrasound by real-time spatiotemporal filtering of ultrafast images », *Phys. Med. Biol.*, vol. 62, p. 31-42, dec. 2016, doi: 10.1088/1361-6560/62/1/31.

[17] K. Christensen-Jeffries *et al.*, « Super-resolution Ultrasound Imaging », *Ultrasound Med. Biol.*, vol. 46, jan. 2020, doi: 10.1016/j.ultrasmedbio.2019.11.013.

[18] P. Song, A. Manduca, J. D. Trzasko, et S. Chen, « Ultrasound Small Vessel Imaging With Block-Wise Adaptive Local Clutter Filtering », *IEEE Trans. Med. Imaging*, vol. 36, nº 1, p. 251-262, jan. 2017, doi: 10.1109/TMI.2016.2605819.

[19] K. A. Ozgun et B. C. Byram, « Multidimensional Clutter Filtering of Aperture Domain Data for Improved Blood Flow Sensitivity », *IEEE Trans. Ultrason. Ferroelectr. Freq. Control*, vol. 68, nº 8, p. 2645-2656, aug. 2021, doi: 10.1109/TUFFC.2021.3073292.

[20] Y. L. Li, D. Hyun, L. Abou-Elkacem, J. K. Willmann, et J. J. Dahl, « Visualization of Small-Diameter Vessels by Reduction of Incoherent Reverberation With Coherent Flow Power Doppler », *IEEE Trans. Ultrason. Ferroelectr. Freq. Control*, vol. 63, nº 11, p. 1878-1889, nov. 2016, doi: 10.1109/TUFFC.2016.2616112.

[21] Y. L. Li et J. J. Dahl, « Coherent flow power doppler (CFPD): flow detection using spatial coherence beamforming », *IEEE Trans. Ultrason. Ferroelectr. Freq. Control*, vol. 62, nº 6, p. 1022-1035, june 2015, doi: 10.1109/TUFFC.2014.006793.

[22] Y. L. Li *et al.*, « Real-Time In Vivo Imaging of Human Liver Vasculature Using Coherent Flow Power Doppler: A Pilot Clinical Study », *IEEE Trans. Ultrason. Ferroelectr. Freq. Control*, vol. 68, nº 9, p. 3027-3041, sept. 2021, doi: 10.1109/TUFFC.2021.3081438.

[23] P.-C. Li et M.-L. Li, « Adaptive imaging using the generalized coherence factor », *IEEE Trans. Ultrason. Ferroelectr. Freq. Control*, vol. 50, nº 2, p. 128-141, feb. 2003, doi: 10.1109/TUFFC.2003.1182117.

[24] V. Perrot, M. Polichetti, F. Varray, et D. Garcia, « So you think you can DAS? A viewpoint on delay-and-sum beamforming », *Ultrasonics*, vol. 111, p. 106309, march 2021, doi: 10.1016/j.ultras.2020.106309.

[25] P. Song *et al.*, « Accelerated Singular Value-Based Ultrasound Blood Flow Clutter Filtering With Randomized Singular Value Decomposition and Randomized Spatial Downsampling », *IEEE Trans. Ultrason. Ferroelectr. Freq. Control*, vol. 64, nº 4, p. 706-716, april. 2017, doi: 10.1109/TUFFC.2017.2665342.

[26] U.-W. Lok *et al.*, « Real time SVD-based clutter filtering using randomized singular value decomposition and spatial downsampling for micro-vessel imaging on a Verasonics ultrasound system », *Ultrasonics*, vol. 107, p. 106163, sept. 2020, doi: 10.1016/j.ultras.2020.106163.

**10 - Appendix**

This appendix evaluates theoretically the relationships between temporal singular vectors and singular values of SVD and GC SVD, that is, between $\boldsymbol{V}_B$ and $\boldsymbol{V}_M$ and $\boldsymbol{S}_M$ and $\boldsymbol{S}_B$.

First, we can reasonably assume that pixels in each $\boldsymbol{M}_i$ present similar temporal modulations for the blood and the tissue to pixels in $\boldsymbol{B}$. Indeed, if this condition were not true, the channels would be decorrelated along time and DAS beamforming would not produce an exploitable image. In other words, the pixels of the concatenation $\boldsymbol{M}$ of all matrices $\boldsymbol{M}_i$ should have the same temporal modulation as the pixels of $\boldsymbol{B}$. Hence, we should have $\mathrm{V}_M^t \approx \mathrm{V}_B^t$ and $\mathrm{V}_M^b \approx \mathrm{V}_B^b$, where the exponent $t$ denotes the indices of columns in $\boldsymbol{V}_B$ that contain tissue signals and the exponent $b$ denotes the columns with blood signals. However, for the noise, corresponding columns in $\boldsymbol{V}_B$ and $\boldsymbol{V}_M$ cannot be equal because the individual channels $\boldsymbol{M}_i$ do not contain the same noise realizations as the DAS matrix $\boldsymbol{B}$.

For the matrices $\boldsymbol{S}_M$ and $\boldsymbol{S}_B$, we can now consider the Gram matrixes $\boldsymbol{B}^*\boldsymbol{B} \in \mathbb{C}^{n_t,n_t}$ and $\boldsymbol{M}^*\boldsymbol{M} \in \mathbb{C}^{n_t,n_t}$ given that their eigenvalues are the square of the singular values of $\boldsymbol{B}$ and $\boldsymbol{M}$. With the Casorati matrix form of equation (1), it is straightforward to show that the following expressions for matrices $\boldsymbol{B}^*\boldsymbol{B}$ and $\boldsymbol{M}^*\boldsymbol{M}$ hold:

$$\boldsymbol{B}^*\boldsymbol{B} = \left(\boldsymbol{M}_1^* + \cdots + \boldsymbol{M}_{n_e}^*\right)\left(\boldsymbol{M}_1 + \cdots + \boldsymbol{M}_{n_e}\right) = \boldsymbol{C} + \boldsymbol{C_x} \ (A.1)$$

$$\boldsymbol{M}^*\boldsymbol{M} = \left[\boldsymbol{M}_1^* \ldots \boldsymbol{M}_{n_e}^*\right]\left[\boldsymbol{M}_1 \ldots \boldsymbol{M}_{n_e}\right]^T = \boldsymbol{C} \ (A.2)$$

with:

$$\boldsymbol{C} = \sum_{i=1}^{n_e} \boldsymbol{M}_i^*\boldsymbol{M}_i \ (A.3)$$

$$\boldsymbol{C_x} = \sum_{i=1}^{n_e}\sum_{j=1}^{n_e}\left(1-\delta_{ij}\right)\boldsymbol{M}_i^*\boldsymbol{M}_j \ (A.4)$$

where $\delta_{ij}$ is the Kronecker delta with $\delta_{ij} = 0$ if $i \neq j$ and $\delta_{ij} = 1$ if $i = j$.

Hence, we see that the matrix $\boldsymbol{B}^*\boldsymbol{B}$ is equal to the matrix $\boldsymbol{M}^*\boldsymbol{M}$, *i.e.*, $\boldsymbol{C} \in \mathbb{C}^{n_t,n_t}$, plus a perturbation matrix $\boldsymbol{C_x} \in \mathbb{C}^{n_t,n_t}$. Two limiting cases can be identified. If the imaging medium is perfectly coherent, that is, we have $\boldsymbol{M}_i^*\boldsymbol{M}_i = \boldsymbol{M}_i^*\boldsymbol{M}_j$, then $\boldsymbol{C_x} = (n_e - 1)\boldsymbol{C}$ and the matrices $\boldsymbol{B}^*\boldsymbol{B}$ and $\boldsymbol{M}^*\boldsymbol{M}$ have the same eigenvalues up to a constant and so on for the singular values of $\boldsymbol{B}$ and $\boldsymbol{M}$. If the medium is perfectly incoherent, $\boldsymbol{C_x} \to 0$ and $\boldsymbol{B}$ and $\boldsymbol{M}$ have the same eigenvalues. For a more general and realistic case, we can write the detailed expressions of entries of $\boldsymbol{C}$ and $\boldsymbol{C_x}$:

$$C(t_1,t_2) = \sum_{i=1}^{n_e}\sum_{k=1}^{n_x n_z} m_i(k,t_1)\left(m_i(k,t_2)\right)^* \ (A.5)$$

$$C_x(t_1,t_2) = \sum_{i=1}^{n_e}\sum_{j=1}^{n_e}\left(1-\delta_{ij}\right)\left(\sum_{k=1}^{n_x n_z} m_i(k,t_1)\left(m_j(k,t_2)\right)^*\right) \ (A.6)$$

where $m_i(k,t_1)$ and $m_j(k,t_2)$ are the k-th pixels acquired by channels $i$ and $j$ at times $t_1$ and $t_2$.

We see from equations (A.5) and (A.6) that the entries of $\boldsymbol{C}$ and $\boldsymbol{C_x}$ are in fact quite similar quantities. Indeed, the entries of both matrices are the averaged dot products of pixels but estimated using different pairs of channels $i$ and $j$. In fact, if we assume as before that each channel has a similar temporal modulation for pixels of same index, then the matrix $\boldsymbol{C_x}$ can be considered as an approximated version of $\boldsymbol{C}$ and hence the matrix $\boldsymbol{C} + \boldsymbol{C_x}$ should be quite similar to $\boldsymbol{C}$. In other words, the eigenvalues

of $\boldsymbol{C}$ will be minimally perturbated by the addition of $\boldsymbol{C_x}$. Thus, we can assume that $\boldsymbol{B^*B}$ and $\boldsymbol{M^*M}$ have close eigenvalues and so on for the corresponding singular values of $\boldsymbol{B}$ and $\boldsymbol{M}$, that is $\boldsymbol{S_M \approx S_B}$.

Figures A.1 and A.2 are produced from the *in vivo* dataset presented in the Materials and Method section. Figure A.1 shows the absolute value of matrices $\boldsymbol{C}$ and $\boldsymbol{C + C_x}$ for this dataset with corresponding singular values computed with GC SVD and SVD for $\boldsymbol{M}$ and $\boldsymbol{B}$, respectively. The matrices $\boldsymbol{C}$ and $\boldsymbol{C + C_x}$ have been both normalized by their maximum value. We can see that $\boldsymbol{C}$ and $\boldsymbol{C + C_x}$ exhibit very similar entries as they both reflect the same temporal modulation of data. As a result, the singular values of $\boldsymbol{M}$ and $\boldsymbol{B}$ are very close.

The first and second rows of Figure A.2 represent the subspaces corresponding to the singular values with indices $\alpha$ computed with GC SVD and SVD. The subspace corresponding to $\alpha$ = 1 contains mostly tissue signal, the subspace associated with $\alpha$ = 6 contains mostly blood signal, the one with $\alpha$ = 15 contains mostly noise, and the one for $\alpha$ = 9 is a mix between blood and tissue signals. We can see that the images associated with the subspaces 1 and 6, i.e., with tissue and blood, are almost identical for SVD and GC SVD. For subspace 15, a closer look reveals that the noise pattern is not the same between SVD and GC SVD. To better understand these observations, the last two rows of Figure A.2 show the temporal singular vectors of SVD and GC SVD ($\boldsymbol{V_B}$ and $\boldsymbol{V_M}$, respectively) associated with each subspace and also the first 1000 elements of the corresponding spatial singular vectors ($\boldsymbol{U_B}$ and $\left(\sum_{i=1}^{n_e}(\boldsymbol{U_M})_i\right)$, respectively). As assumed in our theory, we can see that the singular vectors of SVD and GC SVD are almost identical for subspaces 1 and 6, i.e., for tissue and blood, but different for subspace 15, i.e., for noise. The differences observed for the noise subspace are due to the fact that the matrices $\boldsymbol{B}$ and $\boldsymbol{M}$ (on which SVD and GC SVD are computed) do not present the same noise realizations for each pixel. Subspace 9, which is a mix between blood and noise, presents a temporal singular vector that begins to be slightly more different between SVD and GC SVD but that remains correlated. This behavior is because the subspace can be seen as a transition between the blood subspace, which has some correlation between channels and hence between the matrices $\boldsymbol{B}$ and $\boldsymbol{M}$, and the noise subspace. Importantly, Figure A.2 supports the assumption that subspaces containing blood and tissue should be very similar between SVD and GC SVD.

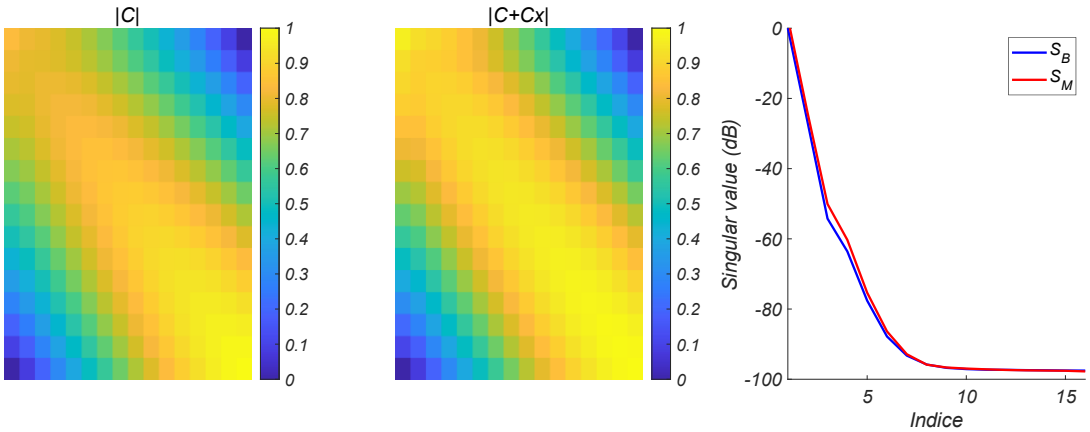


*Figure A.1 – An example of the matrices* $\boldsymbol{C}$ *and* $\boldsymbol{C + C_x}$ *from* in vivo *acquisitions with corresponding singular values in* $\boldsymbol{S_B}$ *and* $\boldsymbol{S_M}$.

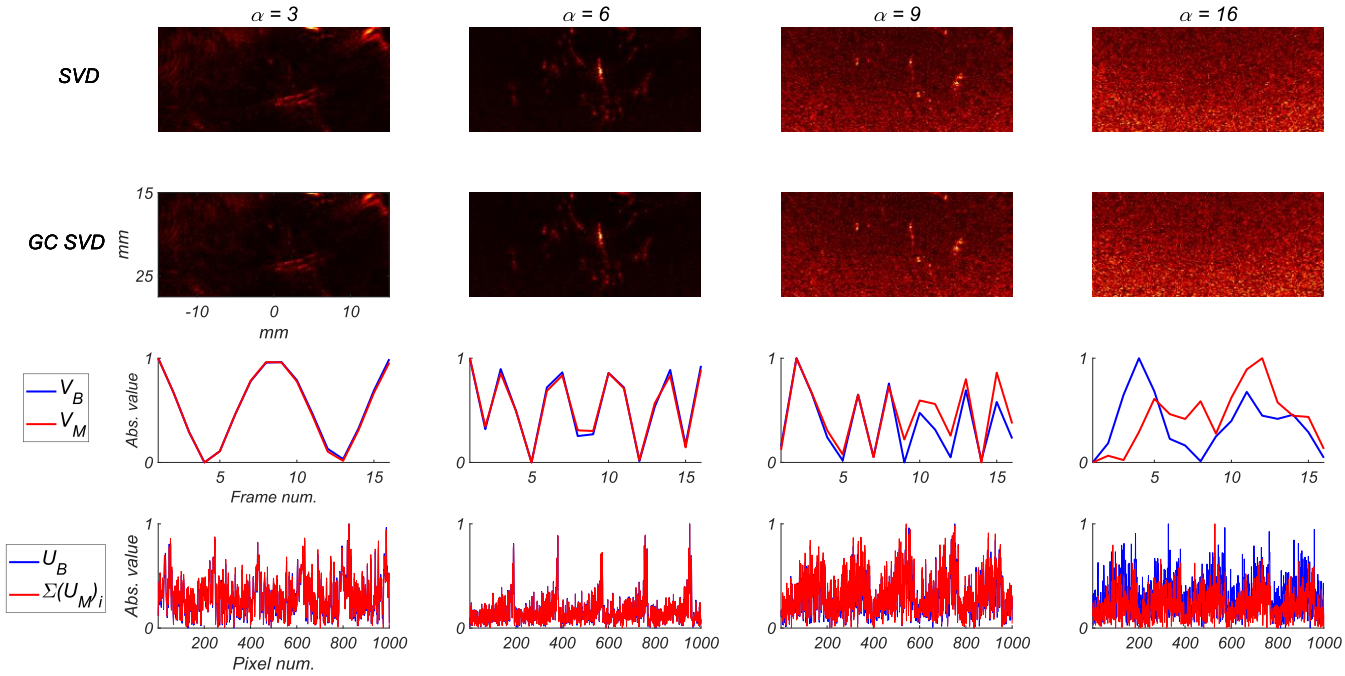


*Figure A.2 – Visualization of some subspaces obtained with SVD and GC SVD from* in vivo *data (the two top rows). Each subspace is denoted by the index α of the corresponding singular value. Singular vectors corresponding to each subspace are also shown (two bottom rows) with* $\boldsymbol{U}_B$ *and* $\boldsymbol{V}_B$ *corresponding to SVD and* $\sum_{i=1}^{n_e}(\boldsymbol{U}_M)_i$ *and* $\boldsymbol{V}_M$ *corresponding to GC SVD.*